

Article

# Geo-Hazard Detection and Monitoring Using SAR and Optical Images in a Snow-Covered Area: The Menyuan (China) Test Site

Qihuan Huang <sup>1,\*</sup>, Yian Wang <sup>1</sup>, Jia Xu <sup>1</sup>, Angelique Nishyirimbere <sup>1</sup> and Zhimin Li <sup>2</sup>

<sup>1</sup> School of Earth Science and Engineering, Hohai University, Nanjing 211100, China; wang.yi.an@hhu.edu.cn (Y.W.); 20080042@hhu.edu.cn (J.X.); itetaange@yahoo.com (A.N.)

<sup>2</sup> Earthquake Administration of Qinghai Province, Xining 810001, China; minhero\_168@126.com

\* Correspondence: insar@hhu.edu.cn; Tel.: +86-25-8378-6961

Received: 12 July 2017; Accepted: 18 September 2017; Published: 21 September 2017

**Abstract:** In this work, we combine SAR and optical images for geo-hazard detection and monitoring in Western China. An extremely small baseline of C-band SAR image pairs acquired from Sentinel-1A at Menyuan, China, is analyzed. Apart from the large area of coseismic deformation, we proposed an earthquake-derived landslide detecting method by removing the coseismic deformation with polynomial fitting, then the detected moving areas were confirmed with Chinese Gaofen-1 optical satellite images. Sentinel-1A C-band interferograms show about a 7-cm line of sight movement caused by the  $M_S$  6.4 Menyuan earthquake; meanwhile, several features indicative of ground movement were detected by the proposed method and demonstrated by the Gaofen-1 optical images; the interpretation of high-resolution optical data complemented the goal of better understanding the behavior of geo-hazard disasters. InSAR time series analysis provides an opportunity for continuous monitoring of geo-hazards in remote areas, while the optical image method is easily affected by decorrelation due to snowfall.

**Keywords:** Menyuan  $M_S$  6.4 earthquake; SAR interferometry; Sentinel-1; Gaofen-1 satellite; geo-hazards

## 1. Introduction

Geo-hazards can cause enormous human and economic losses, as well as environmental disruption. Geo-hazards can be classified into two main categories [1,2]: natural hazards (such as earthquakes, landslides, volcanic eruptions, tsunamis, and floods) and human-induced hazards (such as land subsidence due to groundwater-extraction, water contamination, and atmosphere pollution). Among all natural hazards, earthquakes represent one of the most devastating hazards in terms of economic damage and human suffering, while landslides, which are considered a secondary hazard, cause major infrastructural damages, casualties, and economic losses [3]. Due to the sparse vegetation in the mountainous area of Western China, the surface stability is poor, and landslides and mudslides occur very easily. In earthquake-prone areas, this situation becomes worse. For instance, on 8 August 2010, a large-scale landslide occurred in several valleys in Zhouqu County, China, causing widespread property damage and over 1700 casualties [4,5].

During the past decades, Earth observation (EO), which is the gathering of information about the Earth using remote sensing technologies, has been widely applied to disaster risk management [6], with an exponential increase in geo-hazard applications since the 1990s [1]. Remote sensing can automatically monitor the changes or displacement over the whole land, not only with a few observation points, but with high density and frequency. This technique is very useful and efficient in the field of geo-hazard recognition, monitoring, and forecasting. The advantage of optical remote sensing techniques for geo-hazard monitoring is obviously its visual representation with high resolution [7,8],

while the disadvantage is its inability to work during the night as it is affected by the weather. Synthetic aperture radar (SAR) has the ability to monitor deformation in all weather and with all illumination conditions. However, its resolution is relatively low compared to optical imagery. The demand for automated landslide detection is high, and the approaches using optical images include visual interpretation [9], post-classification comparison [10], image differencing [11], and change vector analysis [12], etc. As far as SAR is concerned for landslide detection, various approaches have been investigated, including the use of interferometric coherence [13], pre- and post- event backscatter information [14], and differential SAR interferometry (DInSAR) [5,14–18] (see Reference [2] for a review of using optical and SAR image data for geological hazard mapping and monitoring).

Decorrelation is one of the challenges of DInSAR technology for landslide detection, which becomes more serious in snow-covered areas. In this work, SAR and optical data are combined for geo-hazard detection and monitoring in snow-covered areas in Western China. We analyze the capability of SAR interferometry (InSAR) using C-band SAR imagery acquired by the European Space Agency (ESA) Sentinel-1A satellite to monitor earthquake-related ground movement. Firstly, large areas of displacement caused by the earthquake were explored using an extremely small baseline Sentinel-1 interferometric pair; then, the coseismic deformation was removed by polynomial fitting in both the range and azimuth directions, and small displacements related to landslides/mudslides/glaciers were achieved, followed by a visual demonstration of optical images from the Chinese Gaofen-1 satellite. Lastly, behaviors of landslides are analyzed by interferometric deformation time series.

## 2. Study Area and Data

According to China Earthquake Network Center (CENC), on 21 January 2016, an  $M_S$  6.4 (surface wave magnitude) earthquake occurred in Menyuan county, Qinghai Province, Western China, with the center of the earthquake, with a depth of about 10 km, located at  $101.62^\circ$  E,  $37.68^\circ$  N. The earthquake was occurred on Qilian Mountain, which is at the northeast edge of the Qinghai-Tibet plate, and expanded across the Qinghai Tibet Plateau to the interior of the continent's forward line. The terrain is particularly complex and intriguing: to the north, there are two deserts named Badain Jaran Desert and Tengger Desert; the Loess Plateau is located to the southeast. The study area is sparsely vegetated, ecologically fragile, and easily affected by geo-hazards. Figure 1 shows the geographic location of the earthquake and the coverage of the descending Sentinel-1A SAR image. The dashed white rectangle outlines the burst for interferometric processing.

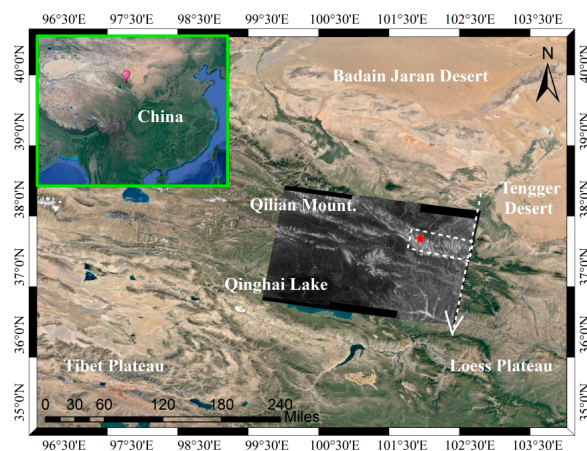


**Figure 1.** The geographical location of the Menyuan earthquake. A descending Sentinel-1A SAR image acquired on 18 January 2016 is superimposed on a GoogleMaps™ image; the dashed rectangle shows the burst for interferogram generation, the red star marks the  $M_S$  6.4 Menyuan earthquake epicenter.

Since 1927, more than five earthquakes with  $M_S > 6$  have occurred within a 100-km range from the epicenter of the Menyuan earthquake, according to the U.S. Geological Survey (USGS). The largest one, with a magnitude of MS 8.0, occurred in May 1927, and the next largest earthquake with a magnitude of MS 6.5 occurred on 26 August 1986 [19]. The easternmost Qilian Mountain called Lenglongling, which is a famous geological fault belt, reflects all the characteristics and essence of the Qilian Mountains; the detailed tectonic background can be found in Reference [19]. The peak of Lenglongling, known as “Gangshika”, a tourist attraction, is 5254.5 m above sea level. It is the main mountain of Qilian Mountain, and the glacier-covered area above 4500 m is about 81 km<sup>2</sup>. Figure 2 shows the study area subtracted from an RGB (band 4, band 3, and band 2) colored image acquired by Sentinel-2A on 8 February 2016, 18 days after the earthquake. The red rectangle illustrates the area covered by the burst of the Sentinel-1A descending image. The region is in a mountainous area and more than 80% was covered with snow. The blue dashed rectangles show the footprint of the Gaofen-1 optical images, and the red star is the earthquake epicenter reported by CENC. The green dashed rectangle marks the research area.

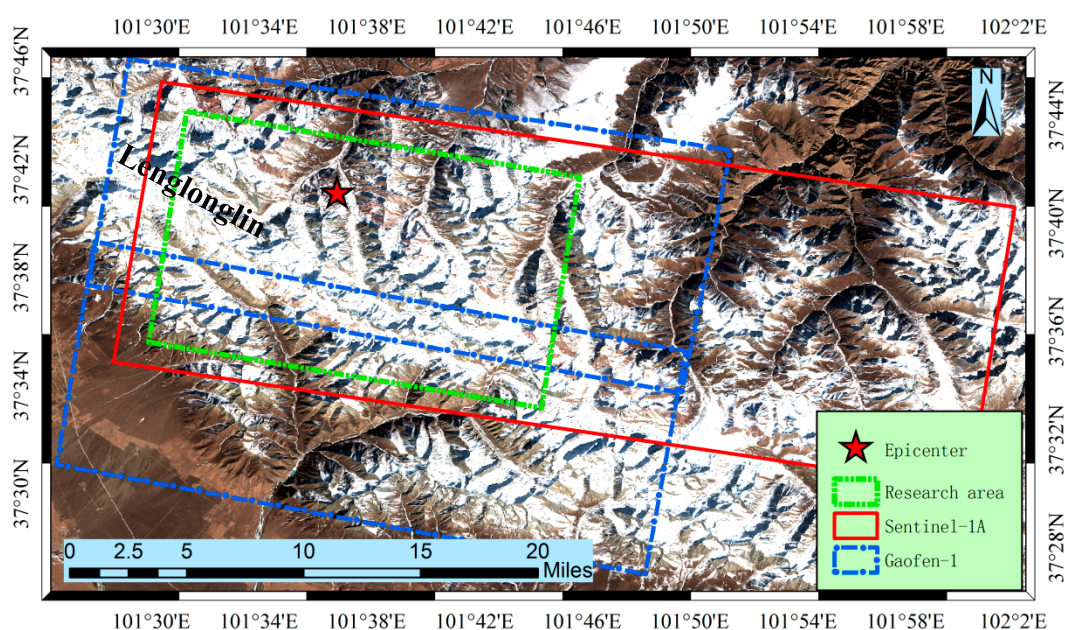


**Figure 2.** Sentinel-2A image acquired on 8 February 2016 showing the Menyuan earthquake area. The red star illustrates the proximate seismic center; the blue dashed rectangles show the footprint of Gaofen-1 optical images; the red rectangle is the Sentinel-1A burst area.

Eleven TOPS (Terrain Observation by Progressive Scan) IW (Interferometric Wide swath) mode SAR images acquired by Sentinel-1A covering a time span from 29 April 2015 to 11 February 2016 were collected (see Table 1); one of the bursts in the first swath, with an incidence angle of 30–36 degrees covering the entire earthquake area, was processed (see the red rectangle in Figure 2). Two Gaofen-1 optical images covering the study area were acquired after the earthquake (8 February 2016) (see the blue rectangles in Figure 2). Gaofen-1 is a Chinese high-resolution optical remote sensing satellite, launched on 26 April 2013, working in a sun-synchronous recursive orbit with a repetition cycle of four days. Gaofen-1 is equipped with a multispectral scanner with the highest resolution of 2 m; more information about the Chinese Gaofen-1 satellite system can be found in Reference [20].

**Table 1.** Sentinel-1A IW mode SAR images pairs for interferometry.

No.	Master Date	Slave Date	Bperp/m	Btemp/d
1	29 April 2015	23 May 2015	−77	24
2	23 May 2015	10 July 2015	−75	48
3	10 July 2015	27 August 2015	166	48
4	27 August 2015	20 September 2015	−101	24
5	20 September 2015	14 October 2015	81	24
6	14 October 2015	1 December 2015	−23	48
7	1 December 2015	25 December 2015	73	24
8	25 December 2015	18 January 2016	−128	24
9 *	18 January 2016	11 February 2016	11	24
10	11 February 2016	6 March 2016	80	24

\* The Ms 6.4 Menyuan earthquake occurred on 21 January 2016.

### 3. Data Processing and Analysis

#### 3.1. Coseismic Deformation Measured by SAR Interferometry

Concerning the exploitation of the SAR interferometric information, there are three different approaches: the classical DInSAR analysis based on single interferograms, the simplified PSI (Persistent Scatterer Interferometry) approach based on temporally-consecutive interferograms, and the full PSI approach which exploits redundant interferograms (with short and large temporal baselines), see, e.g., References [21,22]. The simplified PSI approach is appropriate for non-urban areas, where the maximum coverage is achieved by exploiting the shortest temporal baselines. By contrast, the full PSI approach is indicated to process urban areas, where the coherence loss to temporal decorrelation is less important. In our case, a classical two-pass DInSAR processing chain, developed at the Centre Tecnològic de Telecomunicacions de Catalunya (CTTC), was applied to the Menyuan earthquake deformation monitoring, and the USGS SRTM3 DEM [23] was used for topography removal. A multi-look of five was applied in the range direction to obtain a similar pixel dimension as in the azimuth direction. Taking advantage of the reduced Sentinel-1A orbital tube (the perpendicular baseline is 11 m for the coseismic deformation interferometric pairs, see Table 1), the residual topographic component is disregarded for the classical two-pass DInSAR approach.

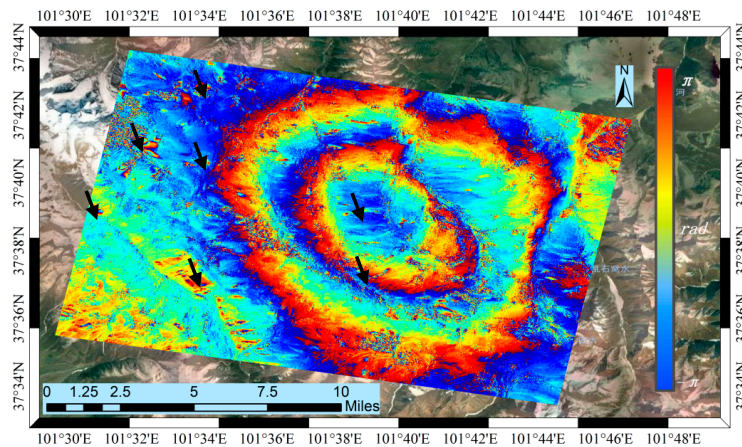
To be addressed, due to the TOPS characteristics, Sentinel-1A data needs extra processing with respect to the standard StripMap processing [24]. This mainly affects the image co-registration step, which is due to a high Doppler rate caused by the azimuth antenna beam steering, which needs to be very accurate (1/103 pixels in azimuth [25]). To achieve such accuracy, a two-step process was proposed: first, a pixel-level co-registration by using the classical SAR image co-registration method, achieved using orbit information and, finally, a refinement of the accuracy by using spectral diversity [24,25].

Figure 3 shows the differential interferogram generated with the Sentinel-1A images acquired on 18 January 2016 and 11 February 2016. More than two fringes can be clearly interpreted, and an unwrapped phase shows a maximum uplift of about 16 rad (see Figure 5), which corresponds to about 7 cm in the radar line of sight direction, and more detailed deformation information caused by this earthquake can be found in References [19,26]. Apart from the large area of deformation caused by the earthquake, small fringe patterns can be clearly seen in the earthquake deformation area (some of them are marked with black arrows in Figure 3).

#### 3.2. Method of Geo-Hazard Detection

In order to locate secondary geo-hazards caused by the earthquake, visual interpretation of the interferogram by looking for the interferometric pattern in the generated coseismic interferogram is a straight choice, while this method is time-consuming and may miss key information in such a large area (more than 400 km<sup>2</sup>). In this case study, a method for fast and automatic geo-hazard detection

based on the single differential interferogram is proposed: firstly, the differential interferogram is unwrapped based on the pixels whose coherence are larger than 0.3 (due to the extremely small baseline, these pixels account for 96.47% in the measured area); secondly, an interpolation procedure based on the Delaunay triangulation is applied to fill the pixels with a coherence lower than 0.3, followed by a fourth-order polynomial to fit the phases in both range and azimuth direction, and their mean values are considered as the coseismic deformation phases; thirdly, the difference between the unwrapped phase and the fitted phase is calculated; lastly, a phase threshold of 3 rad is set to the different phases, followed by a median filter with a window size of  $2 \times 2$  pixels, to obtain the potential geo-hazards area. The flowchart of the proposed method is illustrated in Figure 4.



**Figure 3.** Differential interferogram showing the deformation of the Menyuan earthquake. The interferogram is superimposed on an optical image, with one full color cycle representing a difference in phase of  $2\pi$  corresponding to 2.8 cm of the LOS (Line Of Sight) range change. It was generated using two descending Sentinel-1A IW mode images acquired before (18 January 2016) and after (11 February 2016) the  $M_S$  6.4 Menyuan earthquake (21 January 2016).

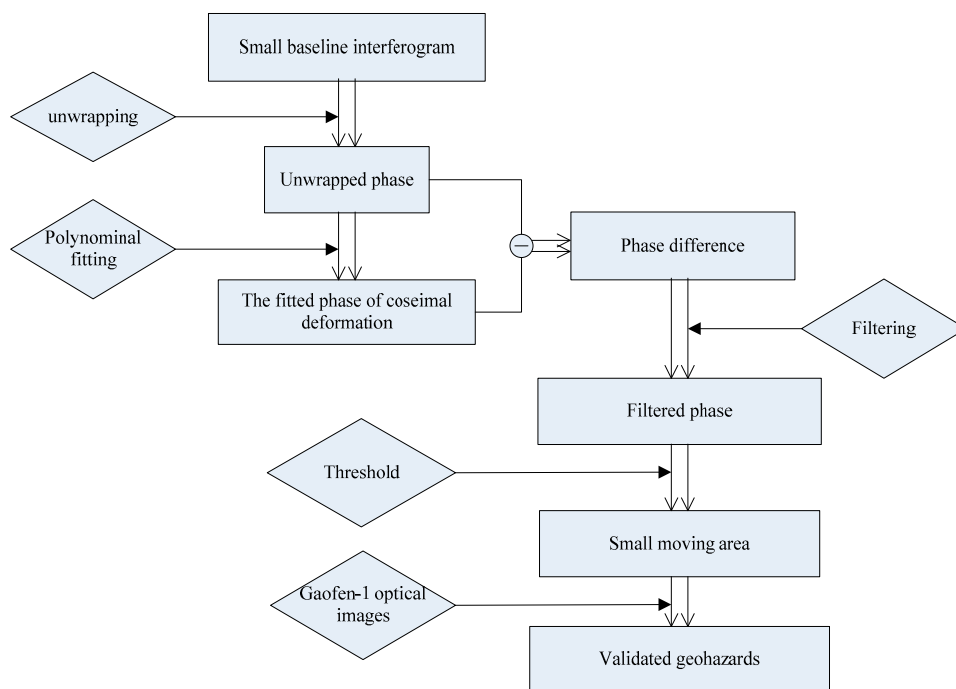


**Figure 4.** The flowchart of geo-hazard area detection based on a single differential interferogram.

Figure 5a shows the unwrapped phase, in which the large deformation area caused by the earthquake is about 16 rad, corresponding to about 7 cm in the line of sight direction. Figure 5b shows the result of the polynomial fitted phase, and the phase difference between the unwrapped and fitted phase is shown in Figure 5c, in which small phase patterns of potential geo-hazard areas can be clearly seen (the black arrows). Figure 6 illustrates the profile (red line in Figure 5a) of the phase difference between the unwrapped and fitted phase. From this figure, small movements of possible geo-hazards can be detected (marked with red ovals).

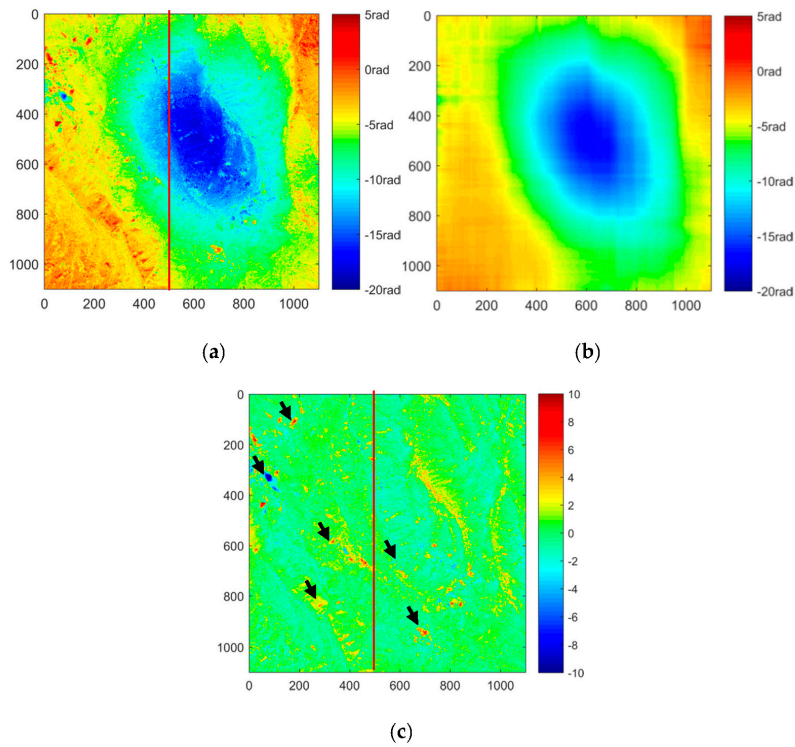


**Figure 5.** (a) Unwrapped deformation phase; (b) phase fitted with a fourth-order polynomial, showing the large area coseismic deformation; and (c) phase difference between (a,b).

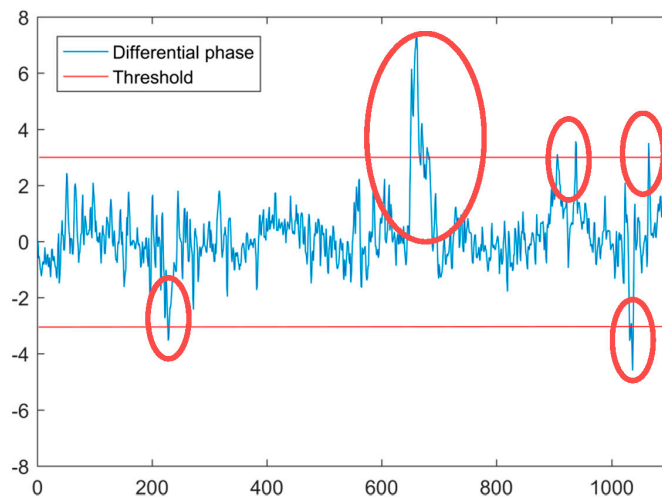


**Figure 6.** An azimuth profile (the red line in Figure 5a) of the difference between unwrapped and the fitted phases; the red lines are the phase thresholds.

### 3.3. Geo-Hazard Detection Results and Validation

Figure 7 shows the areas in which the difference between the unwrapped and the fitted phase is larger than  $\pm\pi$  and possible geo-hazard areas are marked with lowercase letters a–m. To be noted, media filtering with a window size of three was applied before they were superimposed on the optical image. In order to demonstrate the proposed method for geo-hazard detection, optical images of the Chinese Gaofen-1 satellite are used for visual interpretation (see the corresponding images in Figure 8). It can be seen that areas marked with a–e, h–j, and l are glacier movements, while areas labeled with f, g, k, and m are landslides, in which the moving tracks can be seen clearly; area g looks like a mudslide conferring the sliding folds. Due to the limitation of the SAR viewing direction, the proposed method using SAR interferometry for geo-hazard detection can only locate part of the moving areas, which are mainly in the apron slope or back slope. The detecting ability depends on the SAR incidence angle, local slope rate, vegetation, etc.

### 3.4. Deformation Time Series Analysis

Areas g, e, and k were selected for SAR interferometric time series analysis, 10 differential interferograms were generated (see Figure 9) by consecutive image formation with a time span of nearly 10 months, and detailed interferometric parameters can be found in Table 1. In area g, although the interferograms were affected by noise, most of them show a clear shape of the moving area, especially on the top part, interferometric fringes can be detected from blue to red, which means the landslide moves away from the radar in the line of sight direction. In areas e and k, only the last four interferograms show clear interferometric patterns, while the others are strongly affected by noise, considering the rainfall during the monitoring time span (see Figure 9d), and it is clear that the loss of coherence is due to rainfall during the observation.

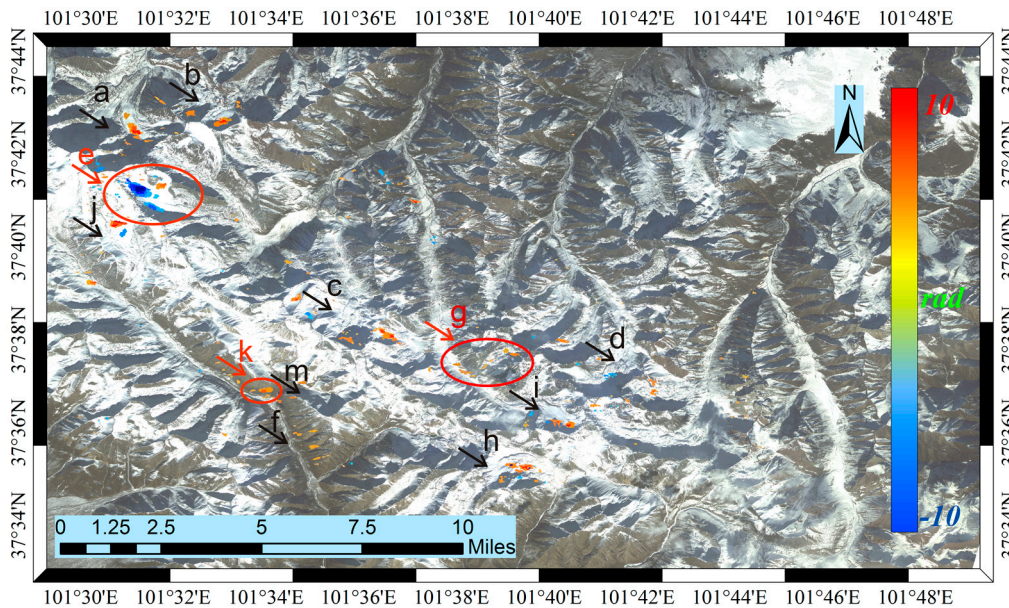


**Figure 7.** Detected possible geo-hazard areas (highlighted with lowercase letters) superimposed on the Chinese Gaofen-1 optical images; the blue color means moving towards the radar, while the red is moving away from the radar, and the arrows show the line of sight direction.

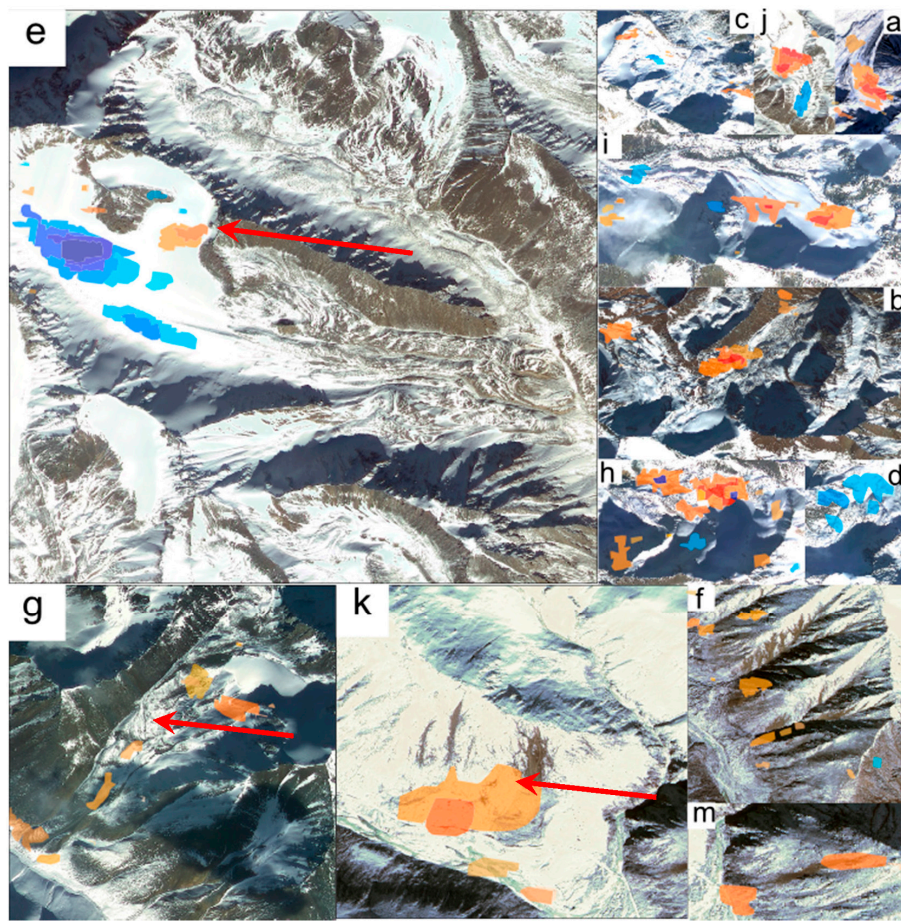


**Figure 8.** Gaofen-1 optical images acquired after the earthquake demonstrate the movements of the corresponding detected area; the radar line of sight is marked with the red arrows.

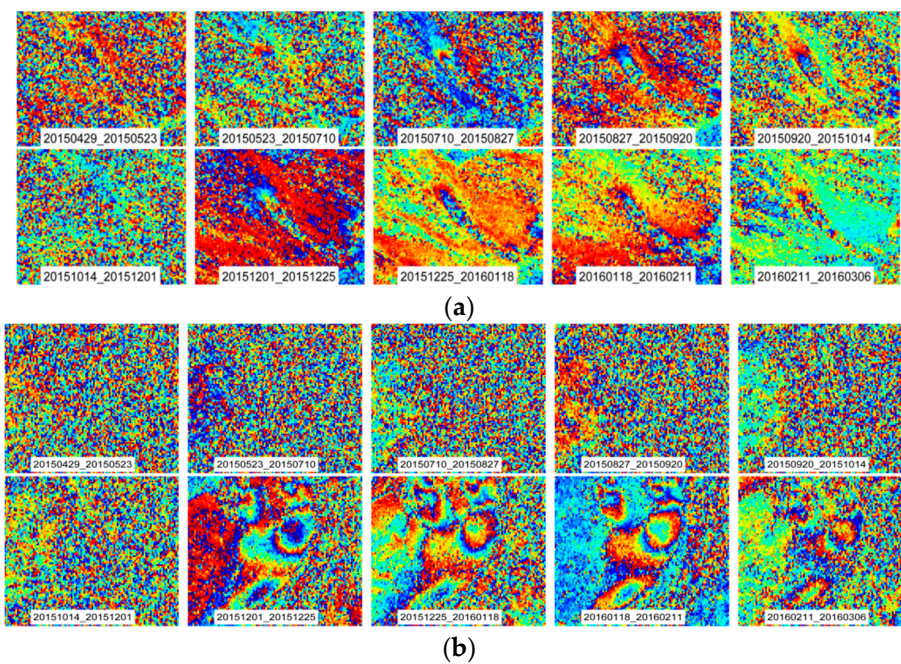


**Figure 9.** Cont.

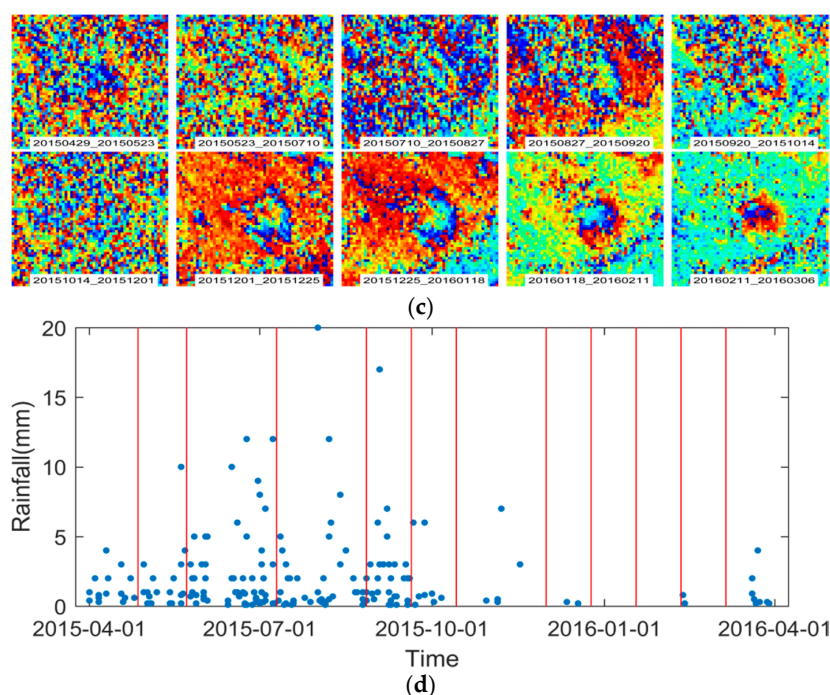


**Figure 9.** Differential interferograms in radar geometry generated with consecutive Sentinel-1A images illustrate land movement at area g (a); e (b); and k (c); the interferograms' dates of master and slave images are given in the bottom; (d) shows the daily rainfall during the monitoring time span, the SAR acquisitions are marked with the red vertical lines.

#### 4. Discussion and Conclusions

This study demonstrates the capability of C-Band Sentinel-1A SAR imagery for detecting and monitoring of ground deformation in the snow-covered area in Qinghai Province, Western China. Apart from the large area coseismic deformation caused by the Menyuan  $M_S$  6.4 earthquake, small ground movements are detected with the extremely small baseline differential InSAR technique, and the results are demonstrated by Chinese Gaofen-1 high-resolution optical images. The combination of the DInSAR interferogram and high-resolution optical remote sensing images can be used for detecting small area ground deformation in snow-covered areas. Moreover, C-band InSAR time series analysis can also be used for the evaluation of geo-hazards, and this technique has great potential for a dynamic geo-hazard assessment and early warning system in Western China; the main decorrelation source is rainfall during the observation time. In addition, the use of remote sensing methods allows for the efficient analysis in large remote areas, making them suitable for investigating geo-hazard processes.

In our test site, with the characteristics of snow-covered high mountains in large areas, ground-based instruments, such as GPS and total stations, cannot acquire sufficient spatial density. In some cases, the instruments cannot even be reached and equipped. In contrast, the remote sensing technique allows for large area observations in a spatially-continuous way, which is especially important in remote places like the west of China, where many landslides/mudslides occur within large areas. The technique is especially useful after an earthquake. Fortunately, the launch of the Sentinel-1 family allows for a regular acquisition of SAR imagery to evaluate the area of interest at a high temporal resolution, and the high resolution of optical remote sensing data is a well-complemented source to assess a specific hazard, like landslides or mudslides. The combination can overcome the disadvantage of InSAR decorrelation related to vegetation and heavy clouds for optical remote sensing.

**Acknowledgments:** This work was supported by the National Natural Science foundation of China (grant no. 41304025, 41301449), and the Natural Science Foundation of Jiangsu Province of China (grant no. BK20130831). We thank the Centre Tecnològic de Telecomunicacions de Catalunya (CTTC) for sharing the SAR interferometric processing tools, and thanks are given to Caleb Iddissah Yakubu from Hohai University for the improvements in English writing. The Sentinel-1A and Gaofen-1 datasets were downloaded from the Sentinel Scientific Data Hub and National mapping Geographic Information Bureau satellite mapping application center, respectively.

**Author Contributions:** Qihuan Huang and Jia Xu conceived and designed the study; SAR data was processed by Qihuan Huang and Yian Wang; Jia Xu and Zhimin Li provided and processed the optical image; Qihuan Huang wrote the paper; Angelique Nishyirimbere reviewed and edited the manuscript.

**Conflicts of Interest:** The authors declare no conflict of interest.

## References

1. Tomás, R.; Li, Z. Earth observations for geohazards: Present and future challenges. *Remote Sens.* **2017**, *9*, 194. [[CrossRef](#)]
2. Joyce, K.E.; Samsonov, S.V.; Levick, S.R.; Engelbrecht, J.; Belliss, S. Mapping and monitoring geological hazards using optical, LiDAR, and synthetic aperture RADAR image data. *Nat. Hazards* **2014**, *73*, 137–163. [[CrossRef](#)]
3. Aleotti, P.; Chowdhury, R. Landslide hazard assessment: Summary review and new perspectives. *Bull. Eng. Geol. Environ.* **1999**, *58*, 21–44. [[CrossRef](#)]
4. Sun, Q.; Zhang, L.; Ding, X.L.; Hu, J.; Li, Z.W.; Zhu, J.J. Slope deformation prior to Zhouqu, China landslide from InSAR time series analysis. *Remote Sens. Environ.* **2015**, *156*, 45–57. [[CrossRef](#)]
5. Sun, Q.; Hu, J.; Zhang, L.; Ding, X. Towards slow-moving landslide monitoring by integrating multi-sensor InSAR time series datasets: The Zhouqu case study, China. *Remote Sens.* **2016**, *8*, 908. [[CrossRef](#)]
6. Poursanidis, D.; Chrysoulakis, N. Remote sensing, natural hazards and the contribution of ESA sentinels missions. *Remote Sens. Appl.* **2017**, *6*, 25–38. [[CrossRef](#)]
7. Le Bivic, R.; Allemand, P.; Quiquerez, A.; Delacourt, C. Potential and limitation of SPOT-5 ortho-image correlation to investigate the cinematics of landslides: The example of “Mare à Poule d’Eau” (Réunion, France). *Remote Sens.* **2017**, *9*, 106. [[CrossRef](#)]
8. Lacroix, P.; Berthier, E.; Maquerhua, E.T. Earthquake-driven acceleration of slow-moving landslides in the Colca Valley, Peru, detected from Pléiades images. *Remote Sens. Environ.* **2015**, *165*, 148–158. [[CrossRef](#)]
9. Domakinis, C.; Oikonomidis, D.; Astaras, T. Landslide mapping in the coastal area between the strymonic gulf and Kavala (Macedonia, Greece) with the aid of remote sensing and geographical information systems. *Int. J. Remote Sens.* **2008**, *29*, 6893–6915. [[CrossRef](#)]
10. Nichol, J.; Wong, M.S. Detection and interpretation of landslides using satellite images. *Land Degrad. Dev.* **2005**, *16*, 243–255. [[CrossRef](#)]
11. Joyce, K.E.; Samsonov, S.; Manville, V.; Jongens, R.; Graettinger, A.; Cronin, S.J. Remote sensing data types and techniques for lahar path detection: A case study at Mt Ruapehu, New Zealand. *Remote Sens. Environ.* **2009**, *113*, 1778–1786. [[CrossRef](#)]
12. Rau, J.; Chen, L.; Liu, J.; Wu, T. Dynamics monitoring and disaster assessment for watershed management using time-series satellite images. *IEEE Trans. Geosci. Remote Sens.* **2007**, *45*, 1641–1649. [[CrossRef](#)]
13. Joyce, K.E.; Dellow, G.D.; Glassey, P.J. Using remote sensing and spatial analysis to understand landslide distribution and dynamics in New Zealand. In Proceedings of the IEEE International Symposium on Geoscience and Remote Sensing IGARSS, Cape Town, South Africa, 12–17 July 2009.
14. Bozzano, F.; Mazzanti, P.; Perissin, D.; Rocca, A.; De Pari, P.; Discenza, M. Basin scale assessment of landslides geomorphological setting by advanced InSAR analysis. *Remote Sens.* **2017**, *9*, 267. [[CrossRef](#)]
15. Ciampalini, A.; Raspini, F.; Lagomarsino, D.; Catani, F.; Casagli, N. Landslide susceptibility map refinement using PSInSAR data. *Remote Sens. Environ.* **2016**, *184*, 302–315. [[CrossRef](#)]
16. Dai, K.; Li, Z.; Tomás, R.; Liu, G.; Yu, B.; Wang, X.; Cheng, H.; Chen, J.; Stockamp, J. Monitoring activity at the Daguangbao Mega-Landslide (China) using Sentinel-1 TOPS time series interferometry. *Remote Sens. Environ.* **2016**, *186*, 501–513. [[CrossRef](#)]
17. Zhang, Y.; Meng, X.; Chen, G.; Qiao, L.; Zeng, R.; Chang, J. Detection of geohazards in the Bailong River Basin using synthetic aperture radar interferometry. *Landslides* **2016**, *13*, 1273–1284. [[CrossRef](#)]

18. Confuorto, P.; Di Martire, D.; Centolanza, G.; Iglesias, R.; Mallorqui, J.J.; Novellino, A.; Plank, S.; Ramondini, M.; Thuro, K.; Calcaterra, D. Post-failure evolution analysis of a rainfall-triggered landslide by multi-temporal interferometry SAR approaches integrated with geotechnical analysis. *Remote Sens. Environ.* **2017**, *188*, 51–72. [CrossRef]
19. Li, Y.; Jiang, W.; Zhang, J.; Luo, Y. Space geodetic observations and modeling of 2016 Mw 5.9 Menyuan earthquake: Implications on seismogenic tectonic motion. *Remote Sens.* **2016**, *8*, 519. [CrossRef]
20. Gaofen-1. Available online: <https://directory.eoportal.org/web/eoportal/satellite-missions/g/gaofen-1> (accessed on 12 September 2017).
21. Devanthery, N.; Crosetto, M.; Monserrat, O.; Cuevas-González, M.; Crippa, B. An approach to persistent scatterer interferometry. *Remote Sens.* **2014**, *6*, 6662–6679. [CrossRef]
22. Crosetto, M.; Monserrat, O.; Cuevas-Gonzalez, M.; Devanthery, N.; Crippa, B. Persistent scatterer interferometry: A review. *ISPRS J. Photogramm.* **2016**, *115*, 78–89. [CrossRef]
23. Rabus, B.; Eineder, M.; Roth, A.; Bamler, R. The shuttle radar topography mission—A new class of digital elevation models acquired by spaceborne radar. *ISPRS J. Photogramm.* **2003**, *57*, 241–262. [CrossRef]
24. Yague-Martinez, N.; Prats-Iraola, P.; Rodriguez Gonzalez, F.; Brcic, R.; Shau, R.; Geudtner, D.; Eineder, M.; Bamler, R. Interferometric processing of Sentinel-1 TOPS data. *IEEE Trans. Geosci. Remote Sens.* **2016**, *54*, 2220–2234. [CrossRef]
25. Prats-Iraola, P.; Scheiber, R.; Marotti, L.; Wollstadt, S.; Reigber, A. TOPS interferometry with TerraSAR-X. *IEEE Trans. Geosci. Remote Sens.* **2012**, *50*, 3179–3188. [CrossRef]
26. Wang, H.; Liu-Zeng, J.; Ng, A.H.-M.; Ge, L.; Javel, F.; Long, F.; Aoudia, A.; Feng, J.; Shao, Z. Sentinel-1 observations of the 2016 Menyuan earthquake: A buried reverse event linked to the left-lateral Haiyuan fault. *Int. J. Appl. Earth Obs. Geoinf.* **2017**, *61*, 14–21. [CrossRef]



© 2017 by the authors. Licensee MDPI, Basel, Switzerland. This article is an open access article distributed under the terms and conditions of the Creative Commons Attribution (CC BY) license (<http://creativecommons.org/licenses/by/4.0/>).